Toward Modular Active-Cell Robots (MACROs): SMA Cell Design and Modeling of Compliant, Articulated Meshes

Ahsan I. Nawroj, *Student Member, IEEE*, John P. Swensen, *Member, IEEE*, and Aaron M. Dollar, *Senior Member, IEEE*

***Abstract*—In this paper, we present the design of a shape-memory-alloy (SMA)-based compliant linear actuator [active cell (AC)] and the use of these in designing and modeling articulated meshes, which form the mechanical subsystem of a class of proposed modular active-cell robots (MACROs). The ACs are capable of undergoing $\sim$25% strain and groups of cells are connected via passively compliant nodes to produce articulated mesh networks. The deformation of compliant meshes of ACs is modeled by scale-invariant parametric equations derived from the physics of SMA deformations and a reduced-order model of the cells. Parameters of the implemented system were used to develop a simulation platform that predicts the mechanical deformation of the networked robot given electrical inputs at arbitrary nodes of the network. We provide results of several experimental trials used to validate and establish the accuracy of this deformation model. The error in predicting deformations in small meshes is shown to be under 10% over both time-varying inputs and at steady states.**

***Index Terms*—Digital material, modular robot, network modeling, networked robot, programmable matter.**

I. Introduction

DISCRETE material robots are an exciting prospect for building redundant, high degree-of-freedom (DOF) articulable structures, such as muscle-like actuators, dynamically adjustable airfoils, continuum manipulators, and others [1], [2], [3]. Discrete material robots use collections of engineered base "elements" that are mechanically connected to form structures that undergo a designed deformation when externally actuated or under passive loads. If the elements are themselves independent actuators, no external force is necessary to drive such mechanisms and their scope can expand to active chassis for mobile robots, articulated robotic skins for social robots, and a wide range of articulated mechanisms, among others.

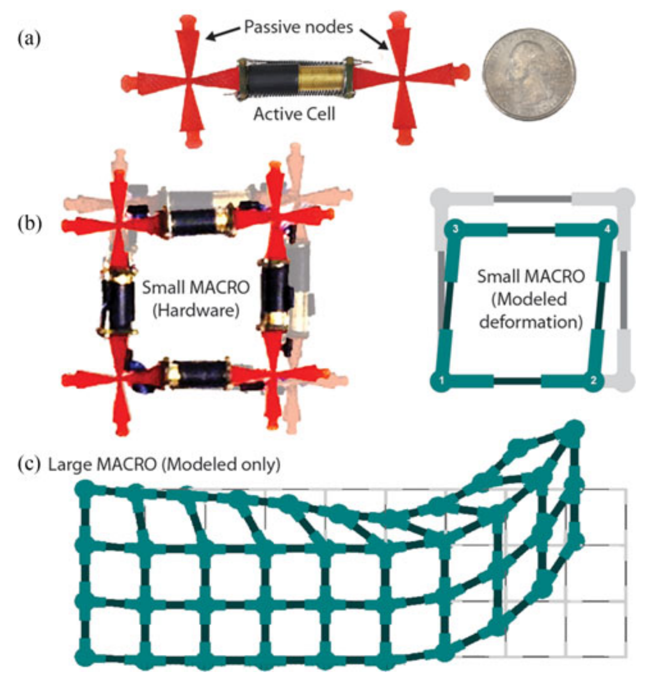

Fig. 1. Example of a MACRO bot acting as a highly articulable support mechanism. The connectivity relations of the smallest units, ACs and nodes (a) as well as the use of strategic power applications to the nodes determine the resulting deformation of the scaffolding structure. Complex patterns of activation of parts of the MACRO (b) result in a desired shape change of the entire mechanism (c). Large systems such as the example shown (initial state in gray and deformed state in green) are modeled using detailed comparisons of the performance of smaller MACRO modules in hardware.

This paper describes the following: 1) an updated design of shape-memory-alloy (SMA)-based active cells (ACs) that miniaturizes the cells and increases strain performance; and 2) the use of ACs and nodes to design-compliant, deformable meshes that are usable in creating a discrete material robot. Our ACs are small, contractile, SMA-based linear actuators (Fig. 1(a), and described in [4]) that can connect mechanically and electrically via compliant flexure nodes to create active, articulated meshes.

Manuscript received October 23, 2016; revised February 21, 2017; accepted April 2, 2017. Date of publication May 3, 2017; date of current version August 7, 2017. This paper was recommended for publication by Associate Editor M. Yim and Editor I.-M. Chen upon evaluation of the reviewers' comments. This work was supported in part by the National Science Foundation under Grant IIS-1317976 and in part by the Air Force Office of Scientific Research under Grant FA9550-11-1-0093. This work was presented in part at the IEEE/RSJ International Conference on Intelligent Robots and Systems, Hamburg, Germany, 2015 [4]. *(Corresponding author: Ahsan Nawroj.)*

A. I. Nawroj and A. M. Dollar are with the Department of Mechanical Engineering and Materials Science, Yale University, New Haven, CT 06520 USA (e-mail: ahsan.nawroj@yale.edu; aaron.dollar@yale.edu).

J. P. Swensen is with the School of Mechanical and Materials Engineering, Washington State University, Pullman, WA 99164 USA (e-mail: john.swensen@wsu.edu).

Color versions of one or more of the figures in this paper are available online at http://ieeexplore.ieee.org.

Digital Object Identifier 10.1109/TRO.2017.2693393

1552-3098 © 2017 IEEE. Personal use is permitted, but republication/redistribution requires IEEE permission.
See http://www.ieee.org/publications_standards/publications/rights/index.html for more information.

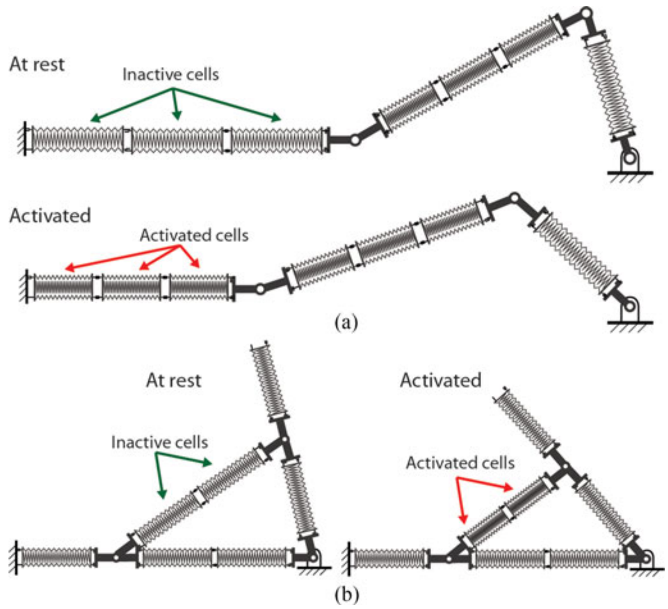

Fig. 2. Diagram of simple application-directed MACROs using our AC design: (a) a crank-slider mechanism and (b) a flexing "arm" created from the same set of ACs and nodes. For each system, the rest and activated states are shown. The systems use the same components to perform very different tasks.

Keeping the vision of discrete material robots in mind, we focus specifically on the shape-changing capabilities of such a robotic device. We believe that the simulated generalized behavior of the proposed robotic device applies to networked and mesh robots in general and will allow more rapid research into such systems. The proposed meshes, combined with external power electronics, control software, and either external or embedded sensors, form a class of systems that we call modular active-cell robots (MACROs). Since the mesh forms the mechanical subsystem of MACROs, in this paper, we refer to MACROs and meshes interchangeably. Additionally, the electronics powering of the MACROs is kept external to the system and external cameras are used as sensors. An example of a small MACRO constructed from four ACs and four nodes is shown in Fig. 1(b). A larger MACRO using many more cells undergoing a flexing motion is shown in Fig. 1(c). This figure highlights the use of our proposed model of simple MACROs to simulate larger structures in a hierarchy of size, complexity, and functionality. Note that the simulated MACROs are all planar and that while the MACRO concept can be readily extended to spatial structures, the mechanical design of such structures for experimentation is significantly more complex. In order to establish the feasibility of accurately simulating MACROs in general, in this paper, we limit all our studies to the simpler, planar meshes.

Like many modular systems, MACROs are particularly useful when application-specific custom parts are not available or accessible to design a mechanism to solve a given task. Additionally, the MACRO paradigm leverages homogeneity of the components to add versatility in their application and reconfigurability to suit changing application demands. This is illustrated in the pair of indicative example MACROs (see Fig. 2), where a flexible "arm" and a rudimentary rocker–slider mechanism is created using nearly identical sets of components. Further, low-level component control may not be necessary when both mechanical connectivity relations as well as power transmission routes are used as design elements. In fact, using many compliant actuators allows MACROs to internally and independently deform under loads and changes in the environment.

The behavior of small MACRO modules can be studied experimentally [4], but larger MACROs are more practically tested in software prior to fabrication and assembly, where the impact of a wide range of parameters such as network connectivity, power connections, and environmental constraints on deformation performance can be thoroughly explored. A robot designer can rely on the known performance of individual MACRO modules to assemble a task-specific robot using various combinations of modules from a library.

This paper is laid out as follows: first, we describe related work in the field (see Section II), followed by a brief description of the design and model of our proposed ACs and nodes (see Section III). Next, we describe the modeling of deformation of compliant, articulated meshes using models of cells and nodes (see Section IV). For MACRO modules that are easily fabricated in the lab, we compared the steady-state and quasi-static deformation of simulated MACROs with experimental hardware trials (see Section V). Finally, we conclude with a summary of the contributions and ideas for future work in designing MACRO bots for given tasks.

II. Related Work

Traditional robots have long, and successfully, used sets of dedicated actuators, linkages, rigid/compliant bodies and on-/off-board intelligence for control and mobility [5], [6]. The prevailing property of these "traditional" robots is the isolation of function into physically separate entities. In the past decade, many modular and reconfigurable robots have been proposed, where control, actuation, and communication are merged in self-sufficient physical blocks [7], [8]. However, even in modular systems, modules remain highly complex and difficult to fabricate in large numbers.

The concept of MACROs is inspired instead by functional biological structures such as cardiac muscle that uses electronic input from pacemaker cells to provide rhythmic tissue activation [9], [10] and the muscle lining of the gastrointestinal tract, which uses structurally simple cells to carry out complex anterograde peristalsis [11]. Although the activation profile of the entire tissue or muscle is complex, it employs patterned activation of largely homogeneous cells. In the human heart, for example, myocardiocytes are simultaneously structural and contractile, capable of contracting individually. In groups, given a stimulation sequence from nearby pacemaker cells, myocardiocytes can form a high-mobility tissue.

Some similarities of our approach can be drawn to programmable matter [12], digital structures, and variable-geometry trusses [1], [13], although these approaches generally suffer from high module complexity and scaling difficulties; hardware-implemented examples are also primarily structural,

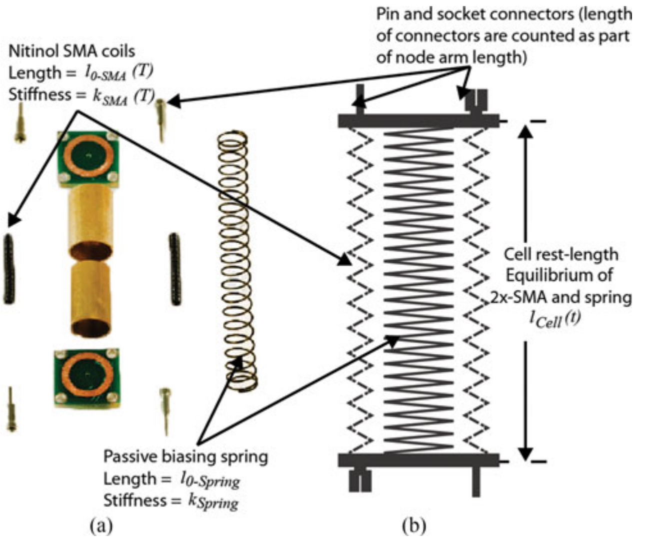

Fig. 3. (a) Cell design showing the components used in fabrication. (b) Parameters of the cell design are labeled for reference for the equations described in the paper.

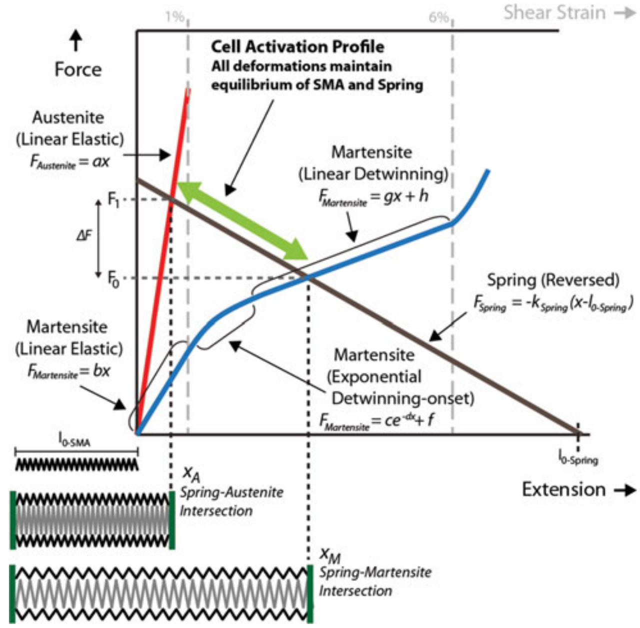

Fig. 4. Typical profile of the SMA used in the cell construction. The design of the cell is optimized to maximize cell stroke through careful choice of the SMA coil and passive spring parameters.

and external actuators are needed to add mobility. Internally actuated deformation is described by Shaw and Hopkins [14] using a large number of custom actuators for relatively low structural deformation. The similarity of these approaches suggest an underlying generalization that we propose is the MACRO: the robots described in [14] can be framed in the MACRO concept using ACs that connect with each other directly without using nodes. In general, all MACROs use simple and rapidly replicable components to create self-actuated, compliant and reconfigurable structures, thus providing the benefits of intelligently designed custom digital structures while allowing for electronic control of their deformation.

Most pioneering work in reconfigurable robots includes the development in tandem of custom simulators [15]. General-purpose robotic simulators for systems of relatively few subcomponents have been described in recent years, including Gazebo [16], Player/Stage [17], and Microsoft Robotics Studio [18]. As the number and complexity of intermodule connections increase, these simulators become increasingly more inaccurate and inefficient [19]. We believe our approach to modeling and simulating MACROs in the general case and employing a multiphysics approach to electrical, thermal and mechanical processes will help accelerate the design and study of many other robots in the future with potentially significantly different designs of ACs.

III. Design and Modeling of ACs and Nodes

A. Design and Modeling of the AC

Our proposed AC is a simple, scalable linear actuator consisting of a pair of coils made from Nitinol SMA secured between two conductive fiberglass printed-circuit boards [see Fig. 3(a)]. When a voltage is applied across the terminals of the cell, the SMA coils are activated through resistive heating and revert to their memory shape of tightly packed coils. The two SMA coils are soldered to the conductive end caps and thus act as parallel extension springs in the assembled cell [see Fig. 3(b)]. A passive compression spring in parallel with the SMA coils provides a bias force to the SMA that restores the cell to its equilibrium position when the driving current is turned off and the SMA is cooled. The effect of this antagonistic setup is illustrated in Fig. 4. A pair of telescoping brass tubes serves as a bearing surface for the spring and prevents the spring from buckling during the duty cycle. The simple arrangement of parts in the AC allows for reliable repetitions of its operation, with 25% repeatable linear strain (up to 28% at peak), contracting fully in $\sim$2 s (for input current of 1.5 A). In general, SMA coils can be activated at higher currents and faster contractions, but we chose to use smaller currents in our design to limit power consumption and allow simultaneous drive to large number of cells.

Resistive heating causes a material transition in the SMA from martensitic to austenitic phrase [20]. The assembly of the cell ensures that in the rest (cold martensitic) state, the SMA coils are in extension and at equilibrium with the passive spring. Above a certain temperature brought about by Joule heating, the coils transition to the hot austenite phase, where the rest length of the SMA coils return to a "memory" shape of close-packed coils. The transition of SMA coil rest length (and corresponding stiffness) shows a predictable hysteresis. The transition temperatures are empirically obtained: cold martensitic coils transition to austenite beginning at T_{As} and completes this transition at $T_{Af} > T_{As}$; hot austenitic coils cool to begin transition to martensite at T_{Ms} and completes transitions at $T_{Mf} < T_{Ms}$ [21]. Although the transition is nonlinear, it can be approximated by a piecewise-linear profile, as shown in Fig. 5. Note that this piecewise-linear profile is obtained by experimentally testing single SMA coils for rest length and stiffness transition

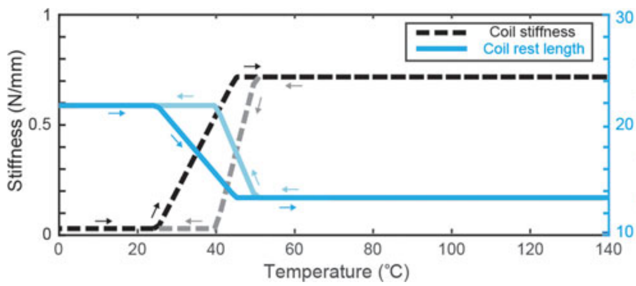

Fig. 5. Mapping functions for rest length and stiffness of SMA coil for a given temperature (approximated piecewise-linear maps for a coil taken from the AC). The temperature is computed for Joule heating of the SMA coils given a time-varying current input. Note the hysteretic response of both stiffness and rest length is shown with arrows as temperature is increased and then decreased.

as Joule heating causes temperature changes, described in [4]. The transition temperatures are found to match the specifications from the manufacturer [21].

To account for the inherent hysteresis of SMA coils, we use two separate models, given the state of the coils. When the SMA coil is in cold martensite state, at a given temperature T

$$l_{0_{\mathrm{SMA}}}(T) = \begin{cases} l_{0,M}, & T \le T_{As} \\ l_{0,M} - a_1 (T - T_{As}), & T_{As} < T \le T_{Af} \\ l_{0,M} - a_1 (T_{Af} - T_{As}), & T > T_{Af} \end{cases} \tag{1}$$

$$k_{\mathrm{SMA}}(T) = \begin{cases} k_{M}, & T \le T_{As} \\ k_M + b_1 (T - T_{As}), & T_{As} < T \le T_{Af} \\ k_M + b_1 (T_{Af} - T_{As}), & T > T_{Af} \end{cases} \tag{2}$$

where

$$a_1 = \frac{l_{0,M} - l_{0,\mathrm{A}}}{T_{Af} - T_{As}} \qquad b_1 = \frac{k_A - k_M}{T_{Af} - T_{As}}. \tag{3}$$

Conversely, for a hot SMA coil in austenite state cooling, at a given temperature T

$$l_{0_{\mathrm{SMA}}}(T) = \begin{cases} l_{0,A}, & T \ge T_{Ms} \\ l_{0,A} + a_2 (T_{Ms} - T), & T_{Ms} > T \ge T_{Mf} \\ l_{0,A} + a_2 (T_{Ms} - T_{Mf}), & T < T_{Mf} \end{cases} \tag{4}$$

$$k_{\mathrm{SMA}}(T) = \begin{cases} k_{A}, & T \le T_{As} \\ k_A - b_2 (T_{Ms} - T), & T_{As} < T \le T_{Af} \\ k_A - b_2 (T_{Ms} - T_{Mf}), & T > T_{Af} \end{cases} \tag{5}$$

where

$$a_2 = \frac{l_{0,\mathrm{M}} - l_{0,\mathrm{A}}}{T_{Ms} - T_{Mf}} \qquad b_2 = \frac{k_A - k_M}{T_{Ms} - T_{Mf}}. \tag{6}$$

The parameters a_1, a_2, b_1 and b_2 are empirically determined from the transition temperatures for the chosen brand of SMA. The values of l_0 and k in both austenitic and martensitic states are empirically obtained from force–extension experiments of samples coils (like the experiment shown in Fig. 4). The values of these parameters for our SMA coils are given in Table I.

TABLE I
MECHANICAL AND ELECTRICAL PROPERTIES OF THE ACs

Property		Value
SMA wire diameter (*d*)		0.305 mm
SMA coil inner diameter (*D*)		1 mm
Volume of SMA in coil (v_{Coil})		24.5 mm^3
SMA density (ρ_{SMA})		6.7 g/mm^3
SMA specific heat-capacity (c_{SMA})		0.8360 J/(g·K)
SMA transition temperatures	T_{As}	40 °C
	T_{Af}	50 °C
	T_{Ms}	45 °C
	T_{Mf}	25 °C
SMA transition properties	$l_{0,M}$	24.0 mm
	$l_{0,A}$	14.0 mm
	k_M	0.030 N/mm
	k_A	0.719 N/mm
Passive spring stiffness (k_{Spring})		0.0507 N/mm
Passive spring rest length ($l_{0-Spring}$)		44.5 mm
Cell rest length		18.7 ± 0.6 mm
Cell electrical resistance (R_{Cell})		0.8 Ω
Stroke of a single cell		4.3 ± 0.6 mm

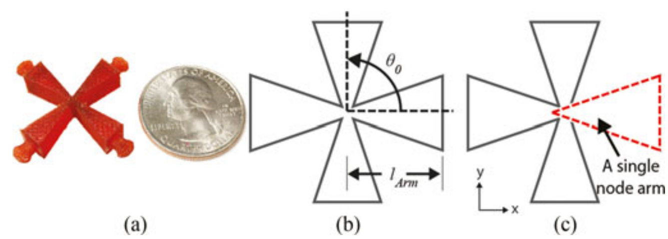

Fig. 6. (a) Modeled polyurethane "flexure" nodes. (b) Notation diagram of the node. (c) A single node arm is marked.

Our prior work [4] establishes a method of computing the optimal set of parameters for the AC, where the rest length of the SMA coils and spring and the stiffness of the spring are varied to optimize the stroke of the cell in a given contraction cycle. Note that while the optimization algorithm from [4] is used, the values in Table I are updated for the altered dimensions of the latest iteration of the AC.

The design parameters selected through this optimization are constrained to increase repeatability by limiting torsional strain in the coils to less than 6% in the martensitic SMA and less than 1% in austenitic SMA [22].

B. Design and Modeling of the Nodes

The nodes in the MACRO concept (see Fig. 6) are compliant revolute joints and serve as electrical inputs to the system. Despite their passive nature, nodes are critical to the design of the MACRO modules since they contribute significantly to the compliance of the structures. Our prior work [4] described nodes made from a set of rigid arms attached to a steel pin. The arms were made from rapidly prototyped acrylonitrile butadiene styrene (ABS) and were thus relatively large compared to the overall size of the ACs. Our latest design of the node uses flexural hinges ("living hinges" [23]) from molded polyurethane [24] to approximate a true revolute joint [see Fig. 7(a)].

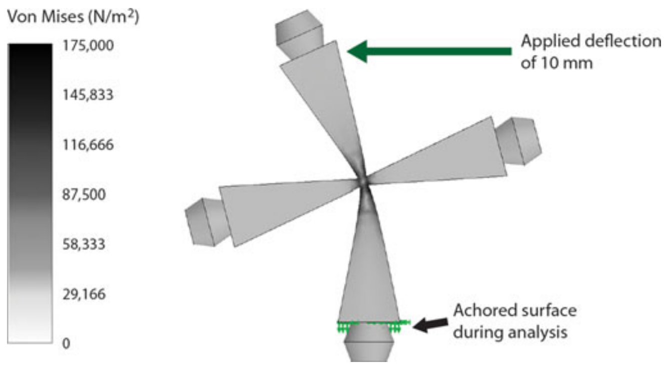

Fig. 7. Stress analysis of a flexure node for a 10 mm deflection in the direction of the marked arrow (large-deflection FEA analysis). The darkest areas (highest stresses) are in a small region near the base of the arms. This supports the approximation of the arm as a rigid body connected to a short-length flexure.

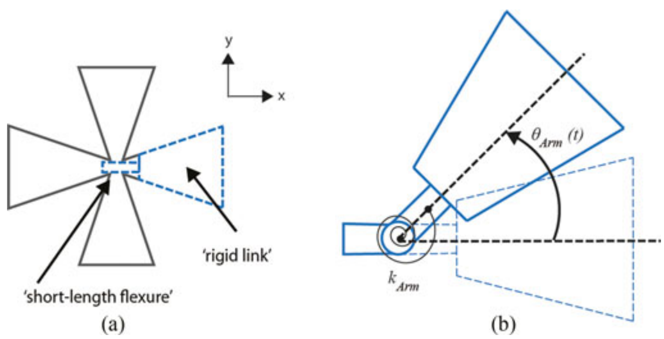

Fig. 8. (a) Simplification of the flexure node for analysis as a short length flexure and a rigid link. (b) Pseudo-rigid-body model of such a node arm at time *t*.

Flexural pivots experience no friction or backlash during rotation but suffer from less easily controlled torsional stiffness. While the rigid arm design could easily be altered to possess different interarm stiffness (attaching different extension springs between arms), the flexure nodes must be remolded with a different geometry. Nevertheless, we believe the low weight, long durability, fewer part count, smaller overall size, and easier replicability of flexure nodes provide a significant improvement in the design.

The torsional stiffness of the flexure pivot is a function of the arm geometry. Fig. 6(b) and (c) shows a section of the used planar arm of a node and a geometrically simplified model of the arm. A finite-element stress analysis for a fixed deflection is shown in Fig. 7 (large deflection nonlinear FEA analysis). Since the bending section of the arm (region of highest stress concentration in Fig. 7) is significantly shorter than the "rigid-link," we can analyze the beam as a short-length flexural pivot in a pseudo-rigid-body model (PRBM) [23]. In this model, the short-length flexural pivot (length *l*) is treated as the chain of two shorter links of length *l*/2 connected by a pin joint. The bending stiffness of the flexural pivot is modeled by a torsional spring at the pin joint (see Fig. 8). The stiffness of the arm (and the torsional stiffness of the modeled spring at the "pseudo-pin") can be written from a linear bending equation

$$k_{\mathrm{Arm}} = {}^{EI_{zz}}\!/_{l}\,. \tag{7}$$

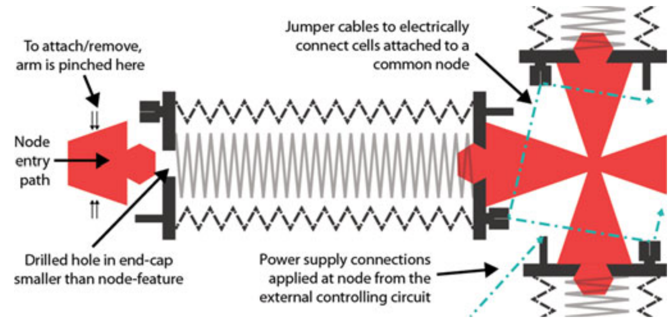

Fig. 9. Connection of passive flexure nodes to ACs. In this implementation, the node arms have a compliant feature that securely attaches to a cell through a drilled hole size smaller than this feature. Removing the node–cell connection requires low forces only if the arm is pinched manually from the side, thus allowing quick disconnection while providing high pull-out forces. The nodes also serve as electrical ports for control currents and as intracell connections (shown as dashed jumper wires). Finally, nodes can be mechanically anchored to the environment to provide constraints to the mesh.

Based on the FEA simulation, we conservatively assume that 10% of the length of an arm is the short-length flexure, while 90% is the rigid link. The modulus of the material *E* is obtained from the manufacturer of the polyurethane. Finally, the moment of inertia of the short-length flexure about the bending axis (out of the page) is I_{zz}, which for a rectangular beam is $bh^3/12$, where *b* is the thickness of the node and *h* is the mean value of the node-arm width along the length of the flexure. Note that for other node designs with distributed stress concentration in bending, the assumptions of PRBM must be verified. In our design, the stiffness of the flexure can be varied by changing I_{zz} (a function of the arm geometry).

Nodes are modeled simply in our system as a set of compliant beams attached to a common pivot. In general, the energy stored in a single node *j* with a set *N*(*j*) neighboring nodes can be written as

$$\Gamma_{\mathrm{Node}_j} = \sum_{k\ \in N(j)} \frac{1}{2} k_{\mathrm{Arm}_k} \left(\theta_{\mathrm{Arm}_k} - \theta_{0_k}\right)^2. \tag{8}$$

Here, each arm j of node i ($j \in N(i)$) stores potential energy from deflection when forces are present on the node arms. The variables θ_{Arm} and θ_0 for each arm are the angle between the arms at a given instance and the rest angle, respectively. The driving forces for these deflections can arise from external disturbances or internal cell actuations in the network.

Although, in general, there can be arbitrary node rest angles and number of arms, for simplicity, we chose θ_0 for the node arms as $2\pi/k$, where $k \,\epsilon\, 1,\, 2,\, \ldots,\, n$ is the number of arms. It should be noted that for practical concerns, the number of nodes *k* is limited by the width of the arms and desired range of motion.

Additionally, each node electrically connects every cell attached to the arms of that node (see Fig. 9). In hardware prototypes, this connection is done through jumper wires; in future work, we aim to incorporate the electrical connection with the mechanical mate of the node arms and cells.

Finally, nodes provide access points for control and power connections to the outside world.

IV. Modeling-Compliant, Articulated Meshes

A. Position and Shape of MACRO Meshes

We define a MACRO mesh as a set Ψ of *m* ACs connected by a set Φ of *n* nodes. The node tuples between which a cell exists is used to generate the mesh, written as the adjacency matrix $A \in \mathbb{R}^{n\times n}$, where $A_{ij} = 1$ if there is a cell between nodes *i* and *j*. The shape of the MACRO mesh is fully defined by the positions of the nodes in space $X = \{x_i \in \mathbb{R}^3 : i \in \Psi\}$. The coordinate system for a single MACRO mesh is relative to a fixed world frame, with its origin at the rest position of node 1.

While modeling planar meshes, we assume that there is no effect of gravity or friction with the environment. Further, we model the shape of the mesh as the quasi-static energy minimal configuration for each cell and node. Essentially, when a cell is activated, the rest length and stiffness of the cell's SMA is altered. This causes a force to be applied on each of the nodes connecting to that cell. By the principle of virtual work, these adjacent nodes move to minimize the potential energy stored in the entire network $(\boldsymbol{\Gamma})$, namely, the energy stored in the SMA coils $(\boldsymbol{\Gamma}_{SMA})$, the passive springs $(\boldsymbol{\Gamma}_{spring})$, and the torsional springs of the node arms $(\boldsymbol{\Gamma}_{node})$.

Formally, the shape of the mesh at any given time is written as

$$X = \underset{X'}{\operatorname{argmin}}\,(\boldsymbol{\Gamma}), \Gamma = \boldsymbol{\Gamma}_{\mathbf{SMA}} + \boldsymbol{\Gamma}_{\mathbf{spring}} + \boldsymbol{\Gamma}_{\mathbf{node}}. \tag{9}$$

Each of these stores of potential energy can be described separately from the connectivity and activation state of the network.

For a given cell *i* connecting nodes *j* and *k* for a given mesh shape X', the cell length l_{cell} can be written as

$$l_{\text{cell}_i} = ||X'_k - X'_j\,||. \tag{10}$$

In general, given the activation of an arbitrary number of cells, the stiffness and rest length of each cell's SMA coil can be at a different value. Thus, the potential energy stored in the SMA coils of the mesh can be written as

$$\boldsymbol{\Gamma}_{\mathbf{SMA}} = \sum_{i\,\in\Psi}\left(k_{\text{SMA}_i}\left(l_{\text{cell}_i} - l_{0_{\text{SMA}_i}}\right)^2\right). \tag{11}$$

Similarly, the energy stored in the springs of the mesh can be written as

$$\boldsymbol{\Gamma}_{\mathbf{spring}} = \sum_{i\,\in\Psi}\left(k_{\text{spring}}\left(l_{\text{cell}_i} - l_{0_{\text{spring}}}\right)^2\right). \tag{12}$$

Let the initial rest shape of the MACRO to be the position set X^0. Then, for a given mesh shape X' and a node *i*, the angle between the *k*th and (*k* + 1)th node arms connecting to node *j* and *k*, respectively, is written as

$$\theta_{\text{Arm}_k} = a\tan\left(\frac{||\left(X'_j - X'_i\right) \times \left(X'_k - X'_i\right)||}{\left(X'_j - X'_i\right)\cdot\left(X'_k - X'_i\right)}\right). \tag{13}$$

The energy stored in all the nodes is the sum of the energy stored in all the node arms for a given mesh shape

$$\boldsymbol{\Gamma}_{\mathbf{node}} = \sum_{j\,\in\Phi}\sum_{k\,\in N(j)}\frac{1}{2}k_{\text{Arm}_k}\left(\theta_{\text{Arm}_k}(t) - \theta_{0_k}\right)^2. \tag{14}$$

TABLE II
Simulation Overview

```
MACRO Simulator
Inputs:
   Initial node positions, x(0), Cell connections, A_ij
   Current inputs, I(t), Node constraints, C_ij
Parameters:
   Cell electrical and mechanical properties (Cell-Model object)
   Node electrical and mechanical properties (Node-Model object)
   Safety limits for cell temperatures, motion limits
Initialize:
   Load Cell-Model, Node-model
   Allocate m networks in variable MACRO using inputs
   for each network N in MACRO do
      Initialize N using input connectivity and positions
   End
Run (timeStep):
   for each network N in MACRO do
      Update node voltages using subarray of I
      for each cell c in N do
         Obtain (power dissipation - cooling power)
         Update cell energy stored over timeStep
         Compute current cell temperature T
         Map T to updated l_0-SMA, k_SMA
      End
      Compute stored elastic potential energy in all cells
      Compute min energy (cells, nodes) node positions
End
Visualize all MACROs simultaneously at the end of the timeStep
```

Note that for any given connectivity of the mesh and set of cell temperatures, the shape of the mesh is possible to obtain through this minimization. We use the MATLAB function *fmincon* to perform this constrained minimization in our simulation.

A list of all the system inputs is given in Table II.

B. Deformation of MACRO Meshes

One of the most important features of the MACRO platform of modular systems is the ability to change the shape of the robotic module, and this is achieved through activation of one or more ACs. In general, there are various methods for achieving this activation, including addressed signals, communication protocols, remote wireless power transmission, etc.

Since our ACs are actuated by Joule heating, the simplest scheme for activating cells in the mesh is to control the power flow through the mesh. We chose to connect current-controlled power supplies to the boundary nodes of our MACRO meshes, which ensures that no internal node connections to the outside world is necessary and allows the system to be scalable.

For a given set of inputs to the nodes, the network is first considered as an electrical resistance network. Analysis of the current dividers setup through the network for given current inputs can be performed using the network Laplacian and Kirchhoff's laws. A description of this analysis method is provided in [25]. To summarize this paper, we can relate the node voltages $\boldsymbol{V}$ to the node currents $\boldsymbol{I}$ for a network with the graph Laplacian $\boldsymbol{G}$ by

$$\boldsymbol{GV} = \boldsymbol{I} \therefore \boldsymbol{V} = \boldsymbol{G}^{\dagger}\boldsymbol{I}. \tag{15}$$

Here, $\boldsymbol{G}$ is the Laplacian of the graph generated using the summed conductance at each node. This method of analyzing node voltages does not use Δ–Y transformations and is generalizable to two-dimensional (2-D) and three-dimensional (3-D) transformations. The graph Laplacian $\boldsymbol{G}$ is not full rank, and thus, the Moore–Penrose pseudoinverse $\boldsymbol{G}^{\dagger}$ is used to compute, for a given vector of node currents, the corresponding voltages at the nodes. The voltage levels are unique up to a scaling factor; this scaling factor is irrelevant for our purposes since the voltage differences are used to compute the power dissipation through the cells as follows:

$$P_{\mathrm{Cell}_i} = (\Delta V_{\mathrm{Cell}_i})^2 \, G_i \tag{16}$$

where the voltage difference across the ith cell is $\Delta V_{\mathrm{Cell}_i}$ and the conductance of the ith cell is G_i.

At each time step k of a simulation trial, the power dissipated across each cell is computed if any of the inputs change over that time step and the heat dissipation across each cell is q_{Cell}

$$q_{\mathrm{Cell}_i} = \int_0^t P_{\mathrm{Cell}_i} \, dt \cong P_{\mathrm{Cell}_i}. \tag{17}$$

With this heat dissipation, for each cell, the temperature of the SMA coils is computed as

$$T = \frac{q_{\mathrm{Cell}\,i}}{\rho_{\mathrm{SMA}} \, v_{\mathrm{coil}} c_{\mathrm{SMA}}} \tag{18}$$

where the material properties (density ρ_{SMA}, specific heat capacity c_{SMA}) are obtained from the manufacturer (Flexinol 0.012”, A_{S} temperature 70 °C actuator wires [21]); volume of the coil v_{coil} is obtained through geometric computation of a tightly packed spring of diameter D and wire diameter d.

The computed temperature of SMA coils is used to update their rest length and stiffness using (1)–(6) described in Section III. This is followed by a constrained minimization of the potential energy of the system per (9)–(14). Finally, an updated node-position set is obtained, describing the shape of the MACRO mesh, given the latest inputs. Note that by construction, the shape deformation is path dependent, since each iteration of the simulation uses the latest position set to begin the new constrained optimization. This is a practical choice for modeling meshes since Nitinol SMA is a low-bandwidth hysteretic actuator and input voltage or current changes do not immediately translate to a cell state change.

It should be noted that the low operational bandwidth of Nitinol SMA is advantageous from an electronics perspective. As the scale of a MACRO grows in number of nodes and cells, the total requisite input currents can be quite large. However, since SMA actuation occurs through Joule heating, the external electronics need not provide high continuous currents but rather multiplex voltage or current inputs at the nodes at a higher bandwidth than the response bandwidth of the SMA. Detailed exploration of this electronics solution is left for future work, and all MACROs constructed and experimentally tested in this paper are powered by dedicated power electronics per node.

The entire algorithm for the computation of node positions for changing inputs is summarized in Table II. Updates to the model of the cells and nodes (using the described equations) occur at every trigger time during the simulation, and the user can elect to apply triggers at an evenly spaced or variable time resolution. When the network state is undergoing little change (inputs unvarying to certain MACRO modules of the entire robot, etc.), frequent triggers is computationally wasteful since the network state is unlikely to change dramatically. An intelligent monitor of inputs is included in the software system that conservatively estimates the necessary physical accuracy and triggers the simulator at higher frequency during times where large dynamic changes occur (e.g., when the input has been changed, when cells have begun to be activated, etc.). It is also possible for the user to select between a “rough estimate” simulation through a low-frequency trigger (e.g., update the MACRO deformation every second) or a highly accurate, and slower, analysis (e.g., update the MACRO deformation every 1/10$^{\text{th}}$ of a second).

Finally, the algorithm in Table II also allows applying motion constraints on nodes, providing the user with the ability to anchor specific nodes or mimic environmental barriers.

C. Control of MACRO Deformation

MACRO deformation can be controlled in two ways—by adjusting the current inputs at the boundary nodes and by varying the initial connectivity of the cells and nodes. The configuration of a MACRO mesh is a critical avenue for control since it helps guide the deformation over all current inputs and alleviates the required electronic control effort.

Note that the control policy, given a specified connectivity of cells and nodes, does not require many sensors. Since the goal is to control the MACRO deformation from the boundary nodes only, we hypothesize that a vision-based system may suffice in this task. In general MACRO systems and AC designs, embedded sensors of temperature, actuation, etc., may be appropriate.

It should be noted that SMA-based ACs require high currents to actuate, and this can present practical obstacles in controlling large MACRO meshes. For a given set of current inputs, however, mesh size only translates to lower bandwidth of operation: a small voltage difference across an AC dissipates a lower amount of power, which causes slower heating of the SMA. For our experiments, we ignore the time to complete actuation, and this allows us to reasonably compare various mesh sizes.

As in all aspects of the MACRO paradigm, the specific actuator and consequent control strategy is not a constant: the described methods and results apply to any actuator that behaves as a contractile element along the edges of the mesh. The choice of actuator and node design is a function of the design constraints for the task that the robot performs.

Currently, our implementation of the simulation solves the forward kinematics problem of computing a network shape, given a time series of input currents. In future work, we will describe an algorithmic solution to the inverse problem of predicting appropriate inputs at the nodes to generate a selected shape.

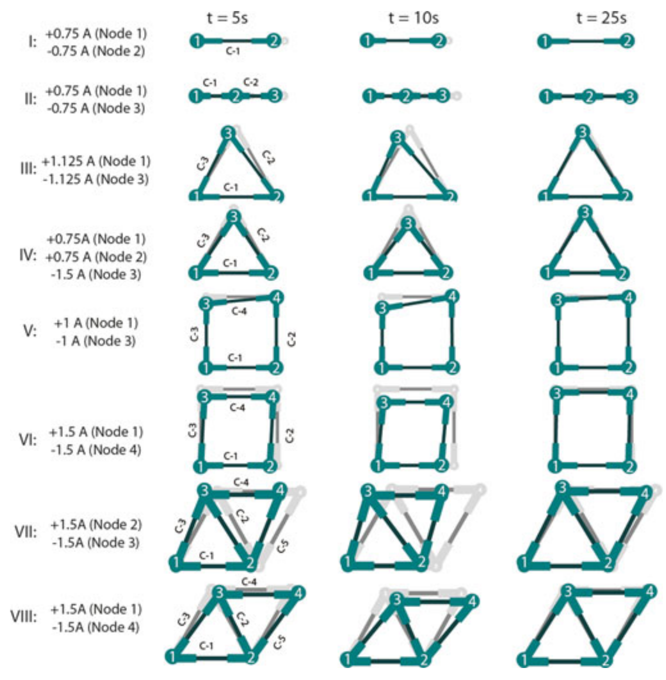

Fig. 10. Visualization as a performance metric of the simulation; animation frames are shown for experimental conditions I–VIII. Three frames per condition show the mesh at 5 s (cells activating), 10 s (activation complete), and 25 s (cells reaching original configuration after power is turned off).

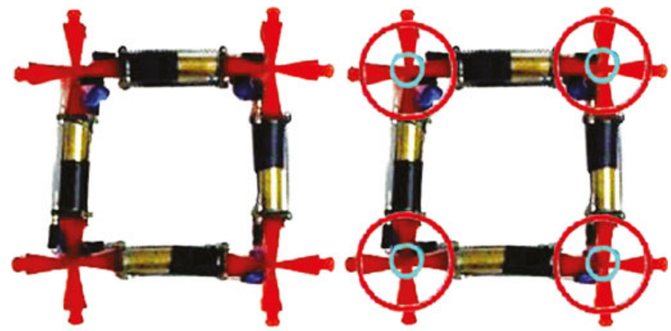

(a) (b)

Fig. 11. Each frame of the trial video is used to extract node-position information: (a) unprocessed frame and (b) identified features.

V. Experimental Validation of the Mesh Model

To use the MACRO mesh model to help design application-specific robotic modules, the model must be validated, especially with changing configurations for a given number of cells and nodes. We fabricated a set of ACs and nodes and assembled them into eight configurations using one or more cells. These configurations were activated by current inputs, and their motion was observed using a computer vision system. For identical configurations and current inputs, MACRO mesh models were simulated and the hardware trials were compared to the corresponding simulation results to show low errors over the course of the trials as well as in steady states of full activation.

A. Experimental Setup

We performed a series of experiments on a small planar MACRO modules to establish the accuracy of mesh modeling. Each of these MACRO modules is placed on a flat table surface with a webcam mounted above the table. A description of the test configurations is listed in Fig. 10, including the breakdown of power activation for a single 30-s trial of each configuration (all trials were run with a fine temporal resolution of 0.1 s between update triggers). Current commands were sent from an Arduino microcontroller to a bank of relays that supply the desired current to the specified nodes of the mesh. For each condition, power was applied to the stated nodes from $t = 0$ to 10 s. At $t = 10$ s, the node power was turned off and cooling fans were turned on for 20 s to complete a single 30-s trial. While SMA coils can be operated at a higher bandwidth, we chose these times to ensure that for the given current inputs (1.5 A through any activated cell), the network would reach a contracted steady state before external cooling was activated. Each network configuration was run for ten trials with identical inputs.

For each hardware trial, we simulated the network configuration with identical inputs, and simulation outputs (node positions) were compared against the corresponding set of hardware trials for errors in node position prediction.

To track the MACRO deformation from videos captured by the webcam, we dyed the flexure nodes a shade of red that is easily segmented in the image frames. A typical image frame from a test video is shown in Fig. 11(a). To identify the positions of the nodes, the image is first undistorted using an experimentally determined camera intrinsic calibration matrix. The undistorted image is thresholded in saturation to isolate the high-saturation red flexures. The resultant binary image is then filtered using a standard erosion-dilation algorithm using a circular disk as a kernel. For any given trial with a known number of nodes in the MACRO (n_{Nodes}), the n_{Nodes} largest connected components in the filtered image are identified. The node centers (intersection of the node arms) are found as the geometric centroid of the arm extreme points. The result of this algorithm is the identification of the nodes in the image frame [see Fig. 11(b)]. This visually identified node position is correlated with simulated node positions for purposes of comparisons of experiments with the simulations.

B. Results and Error Analysis

Outputs of the simulation are visualized as an animation of the MACRO activation drawn using representative lengths of ACs and nodes. At each time step, the node positions are output for further processing. To compare the outputs of the simulation and the trial videos quantitatively, we compared the lengths of the ACs in simulation and the experiments with a world frame origin at Node 1.

The data are analyzed both as a time series and at steady states. The time-series analysis shows how the prediction of the simulation differs from experiments and indicates the level of unmodeled dynamics of the SMA-based mesh. Steady-state comparison shows the accuracy of the modeling equations in predicting deformations.

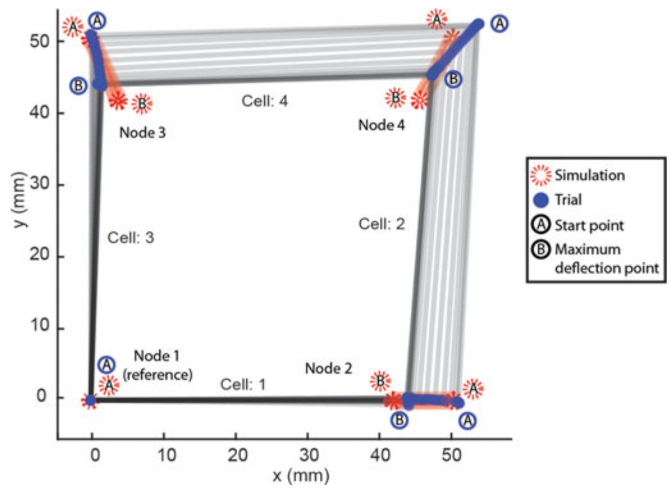

Fig. 12. Comparison of the node trajectory for the nodes of a MACRO. In this example, a trial of the experimental condition III is shown at start (0 s) and at the maximum deflection (15 s).

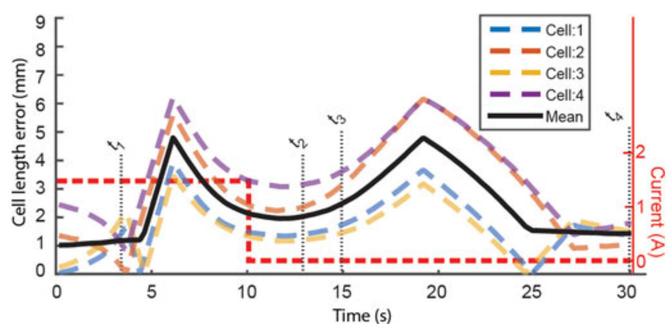

Fig. 13. Cell-length error between simulation and experiment over the course of a trial of experimental condition VI. The "mean" curve shows the average error of the cell lengths. The input is plotted in red (right axis).

1) Temporal Analysis: The hardware trials of these same MACROs can be visualized by plotting the trajectory of the nodes for the simulation and trials. An example of this trajectory comparison for experimental condition III is shown in Fig. 12. This establishes the direction of shape change as similar between simulation and experiments. To compare the dynamics of the system, the trajectory errors for cell length can be plotted as a time series, shown for a representative trial in Fig. 13. Note that the time series of positions will show a high error for modeling inaccuracy as well as time lag in events between simulation and experiments.

2) Steady-State Performance: This is a comparison of the modeling accuracy at steady states of MACRO shape changes. Since the MACRO modules are actuated to achieve a specified shape, for many applications, the intermediate deformations toward a goal shape may not be important. To perform this analysis, we define steady-state positions $X(t_s)$ as the node positions for a steady-state time t_s defined over a time window t_w such that for a small variation tolerance δ

$$t_s : \frac{\partial}{\partial t}\left(X\left(t\right)\right) < \delta \qquad \forall t : \left|t - t_s\right| < \frac{t_w}{2}. \tag{19}$$

The selected window width t_w depends on the frequency of input changes (events); we set $t_w = 3s$ for our analysis. The

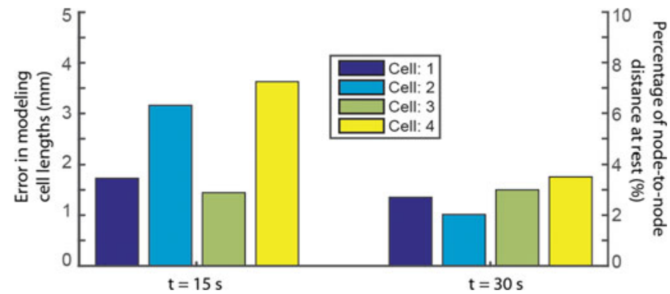

Fig. 14. Comparison of steady-state performance in measured length of each cell in a representative trial (condition VI) of simulation and experiment. Errors are <10% at all times and tend to converge to low values (<2 mm) at the end of trial, attributed to errors in hardware cell fabrication and experimental errors.

tolerance δ is set to 1 mm. Steady-state errors for a representative condition is shown in Fig. 14.

C. Discussion

Several time markers are shown in Fig. 13 to indicate significant transient and steady-state events during the experimental trials. At time t_1, the errors in all node positions show a significant rise. Since current inputs to the system start at $t = 0$ s, this time t_1 represents the first point of divergence between the response of the MACROs and the model. Since current inputs through activated cells is *1.5* A, the actuation time for cells are ∼*2* s. We hypothesize the error peak starting at t_1 is the effect of static friction in experimental system (i.e., between the MACRO and the table), which is not modeled in simulation. A similar effect is seen when the input has been turned off at $t = 10$ s, where the static friction in the deformed module creates a modeling error at time t_2. For applications requiring high transient performance, a model of stiction can be introduced to improve the accuracy of modeling a time lag in the simulated network.

Steady-state errors are evaluated at t_2 and t_4. We hypothesize the steady-state error in cell errors (see Fig. 14) is largely a function of the fabrication inaccuracies of ACs (which are currently fabricated by hand and leads to significant variance between cells) and nodes and will decrease as increased automation is used during the fabrication process. Additionally, the frictional effects described previously exacerbate these errors as well. Steady-state error can also be reduced by individually calibrating each fabricated cell for modeling, but this is not practical as the number of cells in a network increases. The experiments show, however, that the steady-state errors are relatively low (5%–7% in the worst case, shown in Fig. 14). During the entire trial, for all trials, the modeling error in internode distance (modeled cells) remains under 10% of the internode distance [see Fig. 15(a)].

The performance of the modeling equations must be robust to increasing network complexity for the proposed model to be useful. We plotted the trial errors from Fig. 15(a) against the number of cells in the mesh in Fig. 15(b). The mean error (normalized by the cell rest length) is <6% for test conditions; the linear fit of errors shows very little correlation (R-squared of 0.34). This supports the accuracy of the model of individual cells

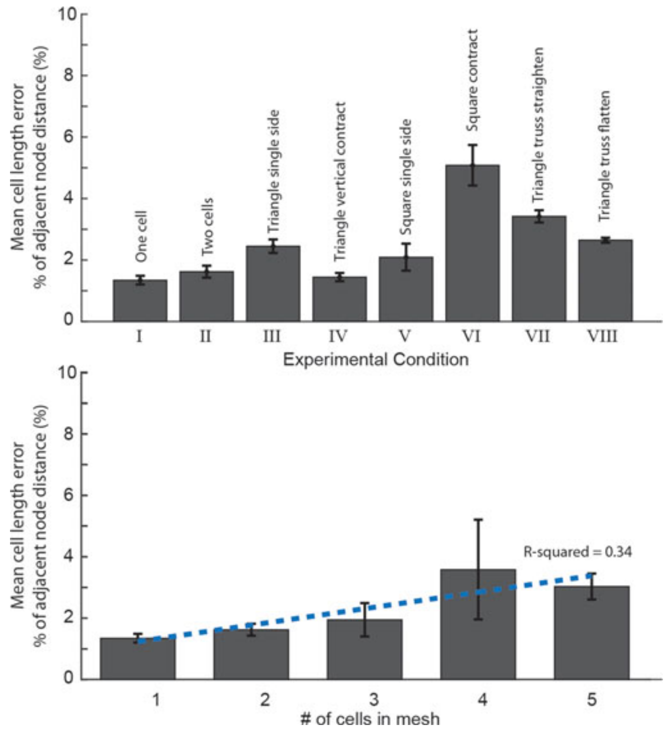

Fig. 15. (a) Mean cell-length errors for all experimental conditions. For all conditions, the mean error over entire trial remains under 10%. (b) Segmentation of errors in experimental conditions by number of cells in the MACRO mesh. Average errors increase slightly with number of cells but is found to be under 5% for all tested systems.

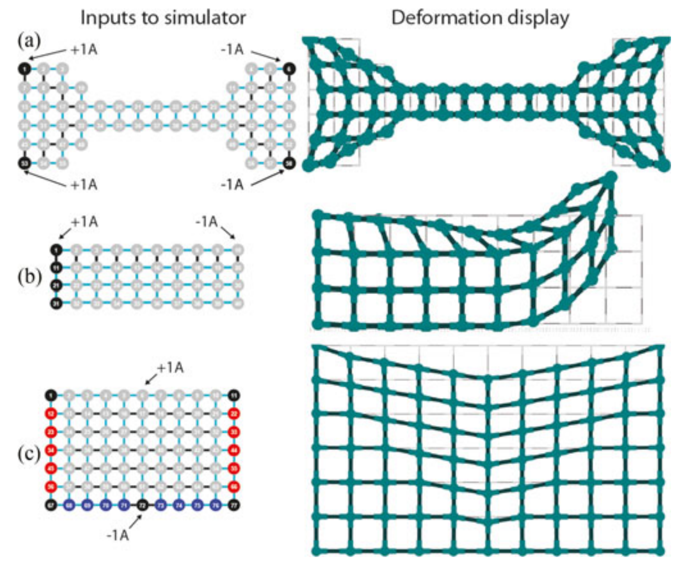

Fig. 16. Summary of the simulations of large MACROs; the variety of examples demonstrate the versatility of the model and the potential of creating application-driven structures using AC networks (inputs on left, outputs on right). In the input images, nodes constrained along the *x*-axis are in red, along the *y*-axis are in blue, and fully anchored nodes are colored black; high-impedance (disconnected) edges are colored black.

regardless of the connectivity of adjacent cells and suggests a low cell internal stress due to deformation of neighboring cells.

Note that the variance of a four-cell mesh has high error variance over the course of trials, and this can be explained through the consideration of network rigidity: kinematically constrained rigid networks such as triangles and trusses show lower error variance, while networks with unconstrained degrees of freedom ("floppy modes"), such as chains of cells and squares, are less accurately modeled. This demonstrates a design principle for MACROs: network simulations are likely to be more accurate for rigid networks, and so designed systems should use rigid networks for high-accuracy systems.

Although a significant number of trials are used in this analysis (80 trials of 30 s each), the number of nodes and cells used in validation is small (largest test samples had only five cells). While the data support the hypothesis about modeling error being low ($< 10\%$), it is insufficient to provide a reliable error law for extremely large networks. However, a simulation platform is important for analyzing any significantly large network, and we believe our results show that the stated modeling effort is sufficient to use as a design tool in this regard.

D. Simulating Large Networks

We highlight the utility of the modeling efforts using some examples of large networks whose performance is simulated using the described platform (see Fig. 16). For each example, we assume a uniform rectangular grid of cells and nodes as the starting material for each application, although our framework supports any cell tessellation. Input constraints are marked on the nodes and edges, respectively, including power connections and motion constraints placed by the simulated environment (nodes with one or more constrained DOFs and one or more virtual walls as "objects").

The results of these simulations support the intuitive deformation for each system and serve to highlight the possibility of creating application-centric structures that can be designed using traditional manufacturing principles while adding functional articulation and potential for reconfiguration. In future work, we aim to explore the targeted design of MACRO meshes that achieve specific tasks.

VI. Conclusion

This paper introduces the design of a simple, contractile, centimeter-scale AC, articulated using a coiled shape-memory alloy actuator. These cells are coupled together via compliant flexure nodes to create networks that we deem MACROs, which can be used to produce highly articulable structures. We formulated a computational model of ACs, passive-compliant connectors and MACRO meshes. We validated these models using several experimental hardware networks. The developed model was shown to accurately predict the deformation of networks of ACs, and some quantitative evidence suggests modeling inaccuracies are independent of network complexity.

In future work, we plan to design a set of "simple machines" from small MACROs and test their hardware implementation against design simulations. We hope to propose a reliable error law that allows predictions of accuracy about even larger systems. Additionally, we plan to use the simulation of smaller MACROs to predict the performance of their combinations, creating an algorithmic method of designing larger systems using smaller, well-modeled subsystems. Finally, the modeling efforts will culminate in a predictive system for computing the inverse problem of finding control inputs that generate a given shape.

REFERENCES

[1] K. C. Cheung and N. Gershenfeld, "Reversibly assembled cellular composite materials," *Science (80-).*, vol. 341, no. 6151, pp. 1219–1221, Sep. 2013.

[2] K. C. Cheung, "Digital cellular solids: Reconfigurable composite materials," *Ph.D. dissertation, Massachusetts Inst. Technol.*, Cambridge, MA, USA, 2012.

[3] T. A. Schaedler *et al.*, "Ultralight metallic microlattices," *Science*, vol. 334, no. 6058, pp. 962–965, Nov. 2011.

[4] A. I. Nawroj, J. P. Swensen, and A. M. Dollar, "Design of mesoscale active cells for networked, compliant robotic structures," in *Proc. IEEE/RSJ Int. Conf. Intell. Robot. Syst.*, Dec. 2015, pp. 3284–3289.

[5] M. Raibert, "BigDog, the rough-terrain quadruped robot," in *IFAC Proc.*, 2008, vol. 17, no. 1 PART 1, pp. 6–9.

[6] L. U. Odhner *et al.*, "A compliant, underactuated hand for robust manipulation," *Int. J. Rob. Res.*, vol. 33, no. 5, pp. 736–752, Apr. 2014.

[7] K. Kotay and D. Rus, "Motion synthesis for the self-reconfiguring molecule," in *Proc. IEEE/RSJ Int. Conf. Intell. Robot. Syst.*, Oct. 1998, pp. 843–851.

[8] M. Park and M. Yim, "Distributed control and communication fault tolerance for the CKBot," in *Proc. ASME/IFToMM Int. Conf. Reconfig. Mech. Robot.*, 2009, pp. 682–688.

[9] M. E. Silverman, D. Grove, and C. B. Upshaw, "Why does the heart beat? The discovery of the electrical system of the heart," *Circulation*, vol. 113, no. 23, pp. 2775–2781, Jun. 2006.

[10] V. Pelouch, I. M. Dixon, L. Golfman, R. E. Beamish, and N. S. Dhalla, "Role of extracellular matrix proteins in heart function," *Mol. Cell. Biochem.*, vol. 129, no. 2, pp. 101–120, Dec. 1993.

[11] G. D. Hirst, "Mechanisms of peristalsis.," *Br. Med. Bull.*, vol. 35, no. 3, pp. 263–268, 1979.

[12] S. C. Goldstein, J. D. Campbell, and T. C. Mowry, "Programmable matter," *Comput. (Long. Beach. Calif).*, vol. 38, no. 6, pp. 99–101, May 2005.

[13] B. Boutin, A. Misra, and V. Modi, "Dynamics and control of variable-geometry truss structures," *Acta Astronaut.*, vol. 45, no. 12, 1999.

[14] L. A. Shaw and J. B. Hopkins, "An actively controlled shape-morphing compliant microarchitectured material," *J. Mech. Robot.*, vol. 8, no. c, p. 21019, Nov. 2015.

[15] M. Yim, D. G. Duff, and K. D. Roufas, "PolyBot: A modular reconfigurable robot," in *Proc. IEEE Int. Conf. Robot. Autom.*, 2000, vol. 1, no. April, pp. 514–520.

[16] N. Koenig and A. Howard, "Design and use paradigms for gazebo, an open-source multi-robot simulator," in *Proc. IEEE/RSJ Int. Conf. Intell. Robot. Syst.*, 2004, vol. 3, pp. 2149–2154.

[17] B. P. Gerkey, R. T. Vaughan, and A. Howard, "The player/stage project : Tools for multi-robot and distributed sensor systems," in *Proc. Int. Conf. Adv. Robot.*, 2003, pp. 317–323.

[18] J. Jackson, "Microsoft robotics studio: A technical introduction," *IEEE Robot. Autom. Mag.*, vol. 14, no. 4, pp. 82–87, Dec. 2007.

[19] M. W. Jorgensen, E. H. Ostergaard, and H. H. Lund, "Modular ATRON: Modules for a self-reconfigurable robot," in *Proc. IEEE/RSJ Int. Conf. Intell. Robot. Syst.*, vol. 2, pp. 2068–2073, 2004.

[20] D. Roy, V. Buravalla, P. D. Mangalgiri, S. Allegavi, and U. Ramamurty, "Mechanical characterization of NiTi SMA wires using a dynamic mechanical analyzer," *Mater. Sci. Eng. A*, vol. 494, no. 1–2, pp. 429–435, 2008.

[21] "FLEXINOL® technical and design data," 2017 [Online]. Available: http://www.dynalloy.com/pdfs/TCF1140.pdf

[22] S.-M. An, J. Ryu, M. Cho, and K.-J. Cho, "Engineering design framework for a shape memory alloy coil spring actuator using a static two-state model," *Smart Mater. Struct.*, vol. 21, no. 5, p. 16, May 2012.

[23] L. Howell, *Compliant Mechanisms*, Hoboken, NJ, USA: Wiley, 2001.

[24] "Smooth-on," 2017 [Online]. Available: http://www.smooth-on.com

[25] J. P. Swensen and A. M. Dollar, "The connectedness of packed circles and spheres with application to conductive cellular materials," *PLoS One*, vol. 7, no. 12, p. e51695, Jan. 2012.

Ahsan I. Nawroj (M'10) received the B.S. degree in electrical and computer engineering from Lafayette College, Easton, PA, USA, in 2008, and the M.S. and M.Phil. degrees in mechanical engineering in 2013 and 2014, respectively, from Yale University, New Haven, CT, USA, where he is currently working toward the Ph.D. degree in mechanical engineering.

His research interests include the design and construction of automation systems and the use of discrete electromechanical cellular systems to create robotic mechanisms.

Mr. Nawroj is a Student Member of the ASME.

John P. Swensen (M'11) received the B.S. degree in electrical engineering from Utah State University, Logan, UT, USA in 2003, and the M.S. and Ph.D. degrees in mechanical engineering at The Johns Hopkins University, Baltimore, MD, USA in 2009 and 2012, respectively.

He was involved in three years of Postdoctoral and Research Scientist work at Yale University, New Haven, CT, USA. He is currently an Assistant Professor with the School of Mechanical and Materials Engineering, Washington State University, Pullman, WA, USA. His research interests include compliant medical devices, continuum robotic devices, and tunably compliant mechanisms.

Aaron M. Dollar (SM'13) received the B.S. degree in mechanical engineering from University of Massachusetts, Amherst, MA, USA in 2000, and the S.M. and Ph.D. degrees in engineering sciences from Harvard University, Cambridge, MA in 2002 and 2007, respectively.

He is currently the John J. Lee Associate Professor of Mechanical Engineering and Materials Science at Yale University, New Haven, CT, USA. He was engaged in two years of postdoctoral research at the MIT Media Lab. His research interests include human and robotic grasping and dexterous manipulation, mechanisms and machine design, and assistive and rehabilitation devices, including upper limb prosthetics and lower limb orthoses.

Prof. Dollar is the recipient of the 2014 NASA Early Career Faculty Award, the 2013 DARPA Young Faculty Award, the 2011 AFOSR Young Investigator Award, the 2010 Technology Review TR35 Young Innovator Award, and the 2010 NSF CAREER Award.